^{92}Zr(n, γ) and (n,tot) measurements at the GELINA and n_TOF facilities

G. Tagliente,[1,*] S. Kopecky,[2] J. Heyse,[2] M. Krtička,[3] C. Massimi,[4,5] A. Mengoni,[6,4] P. M. Milazzo,[7] A. J. M. Plompen,[2] P. Schillebeeckx,[2] S. Valenta,[3] R. Wynants,[2] S. Altstadt,[8] J. Andrzejewski,[9] L. Audouin,[10] V. Bécares,[11] M. Barbagallo,[1] F. Bečvář,[3] F. Belloni,[12] E. Berthoumieux,[12] J. Billowes,[13] V. Boccone,[14] D. Bosnar,[15] M. Brugger,[14] F. Calviño,[16] M. Calviani,[14] D. Cano-Ott,[11] C. Carrapiço,[17] F. Cerutti,[14] E. Chiaveri,[14,12] M. Chin,[14] N. Colonna,[1] G. Cortés,[16] M. A. Cortés-Giraldo,[18] S. Cristallo,[19,20] M. Diakaki,[21] C. Domingo-Pardo,[22] R. Dressler,[23] I. Durán,[24] C. Eleftheriadis,[25] A. Ferrari,[14] K. Fraval,[12] V. Furman,[26] K. Göbel,[8] M. B. Gómez-Hornillos,[16] S. Ganesan,[27] A. R. García,[11] G. Giubrone,[22] I. F. Gonçalves,[17] E. González-Romero,[11] A. Goverdovski,[28] E. Griesmayer,[29] C. Guerrero,[14] F. Gunsing,[12] T. Heftrich,[8] A. Hernández-Prieto,[14,16] E. Jericha,[29] F. Käppeler,[30,†] Y. Kadi,[14] D. Karadimos,[21] T. Katabuchi,[31] V. Ketlerov,[28] V. Khryachkov,[28] N. Kivel,[23] M. Kokkoris,[21] J. Kroll,[3] C. Lampoudis,[12] C. Langer,[8] E. Leal-Cidoncha,[24] C. Lederer,[32] H. Leeb,[29] L. S. Leong,[10] R. Losito,[14] M. Lugaro,[33] A. Mallick,[27] A. Manousos,[25] J. Marganiec,[9] T. Martínez,[11] P. Mastinu,[34] M. Mastromarco,[1] E. Mendoza,[11] F. Mingrone,[4] M. Mirea,[35,†] C. Paradela,[24,2] A. Pavlik,[32] J. Perkowski,[9] J. Praena,[18,36] J. M. Quesada,[18] T. Rauscher,[37] R. Reifarth,[8] A. Riego-Perez,[16] M. Robles,[24] C. Rubbia,[14] J. A. Ryan,[13] M. Sabaté-Gilarte,[18] R. Sarmento,[17] A. Saxena,[27] S. Schmidt,[8] D. Schumann,[23] P. Sedyshev,[26] J. L. Tain,[22] A. Tarifeño-Saldivia,[22] D. Tarrío,[24] L. Tassan-Got,[10] A. Tsinganis,[14] G. Vannini,[4,5] V. Variale,[1] P. Vaz,[17] A. Ventura,[4] M. J. Vermeulen,[38] D. Vescovi,[19,39] V. Vlachoudis,[14] R. Vlastou,[21] A. Wallner,[40] T. Ware,[13] M. Weigand,[8] C. Weiss,[29] T. Wright,[13] and P. Žugec[15]
(n_TOF Collaboration)[‡]

[1]*Istituto Nazionale di Fisica Nucleare, Sezione di Bari, Bari, Italy*
[2]*European Commission, Joint Research Centre (JRC), Geel, Belgium*
[3]*Charles University, Faculty of Mathematics and Physics, Prague, Czech Republic*
[4]*Istituto Nazionale di Fisica Nucleare, Sezione di Bologna, Bologna, Italy*
[5]*Dipartimento di Fisica e Astronomia, Università di Bologna, Bologna, Italy*
[6]*Agenzia Nazionale per le Nuove Tecnologie (ENEA), Bologna, Italy*
[7]*Istituto Nazionale di Fisica Nucleare, Sezione di Trieste, Trieste, Italy*
[8]*Goethe University, Frankfurt, Germany*
[9]*University of Lodz, Lodz, Poland*
[10]*Institut de Physique Nucléaire, CNRS-IN2P3, Université Paris-Sud, Université Paris-Saclay, F-91406 Orsay Cedex, France*
[11]*Centro de Investigaciones Energéticas Medioambientales y Tecnológicas (CIEMAT), Madrid, Spain*
[12]*CEA Irfu, Université Paris-Saclay, F-91191 Gif-sur-Yvette, France*
[13]*University of Manchester, Manchester, United Kingdom*
[14]*European Organization for Nuclear Research (CERN), Geneva, Switzerland*
[15]*Department of Physics, Faculty of Science, University of Zagreb, Zagreb, Croatia*
[16]*Universitat Politècnica de Catalunya, Barcelona, Spain*
[17]*Instituto Superior Técnico, Lisbon, Portugal*
[18]*Universidad de Sevilla, Seville, Spain*
[19]*Istituto Nazionale di Fisica Nucleare, Sezione di Perugia, Perugia, Italy*
[20]*INAF, Osservatorio Astronomico Teramo*
[21]*National Technical University of Athens, Athens, Greece*
[22]*Instituto de Física Corpuscular, CSIC - Universidad de Valencia, Valencia, Spain*
[23]*Paul Scherrer Institut (PSI), Villigen, Switzerland*
[24]*University of Santiago de Compostela, Santiago de Compostela, Spain*
[25]*Aristotle University of Thessaloniki, Thessaloniki, Greece*
[26]*Joint Institute for Nuclear Research (JINR), Dubna, Russia*
[27]*Bhabha Atomic Research Centre (BARC), Mumbai, India*
[28]*Institute of Physics and Power Engineering (IPPE), Obninsk, Russia*
[29]*Technische Universität Wien, Vienna, Austria*
[30]*Karlsruhe Institute of Technology, Campus North, IKP, 76021 Karlsruhe, Germany*
[31]*Tokyo Institute of Technology, Tokyo, Japan*

[*]giuseppe.tagliente@ba.infn.it
[†]Deceased.
[‡]www.cern.ch/ntof

Published by the American Physical Society under the terms of the Creative Commons Attribution 4.0 International license. Further distribution of this work must maintain attribution to the author(s) and the published article's title, journal citation, and DOI.

[32]*University of Vienna, Faculty of Physics, Vienna, Austria*
[33]*Konkoly Observatory Research Centre for Astronomy and Earth Sciences, Hungarian Academy of Sciences, Budapest, Hungary*
[34]*Istituto Nazionale di Fisica Nucleare, Sezione di Legnaro, Legnaro, Italy*
[35]*Horia Hulubei National Institute of Physics and Nuclear Engineering, Magurele, Romania*
[36]*University of Granada, Spain*
[37]*Department of Physics, University of Basel, Basel, Switzerland*
[38]*University of York, United Kingdom*
[39]*Gran Sasso Science Institute, L'Aquila, Italy*
[40]*Australian National University, Canberra, Australia*

(Received 21 February 2020; revised 7 January 2022; accepted 7 February 2022; published 24 February 2022)

Background: Stellar nucleosynthesis of elements heavier than iron is driven by neutron capture processes. ^{92}Zr is positioned at a strategic point along the slow nucleosynthesis path, given its proximity to the neutron magic number $N = 50$ and its position at the matching region between the weak and main slow processes.
Purpose: In parallel with recent improved astronomical data, the extraction of accurate Maxwellian averaged cross sections (MACSs) derived from a more complete and accurate set of resonance parameters should allow for a better understanding of the stellar conditions at which nucleosynthesis takes place.
Methods: Transmission and capture cross section measurements using enriched ^{92}Zr metallic samples were performed at the time-of flight facilities GELINA of JRC-Geel (BE) and n_TOF of CERN (CH). The neutron beam passing through the samples was investigated in transmission measurements at GELINA using a Li-glass scintillator. The γ rays emitted during the neutron capture reactions were detected by C_6D_6 detectors at both GELINA and n_TOF.
Results: Resonance parameters of individual resonances up to 81 keV were extracted from a combined resonance shape analysis of experimental transmissions and capture yields. For the majority of the resonances the parity was determined from an analysis of the transmission data obtained with different sample thicknesses. Average resonance parameters were calculated.
Conclusions: Maxwellian averaged cross sections were extracted from resonances observed up to 81 keV. The MACS for $kT = 30$ keV is fully consistent with experimental data reported in the literature. The MACSs for $kT \lesssim 15$ keV are in good agreement with those derived from the ENDF/B-VIII.0 library and recommended in the KADoNiS database. For kT higher than 30 keV differences are observed. A comparison with MACSs obtained with the cross sections recommended in the JEFF-3.3 and JENDL-4.0 libraries shows discrepancies even for $kT \lesssim 15$ keV.

DOI: 10.1103/PhysRevC.105.025805

I. INTRODUCTION

Neutron capture cross sections are important for nuclear astrophysics and nuclear energy technology. The production of the elements heavier than iron arises almost exclusively from neutron capture stellar nucleosynthesis processes [1–3]. Star temperatures and neutron densities drive the formation of chemical elements through different paths. In supernova explosions or merging neutron stars scenarios, extremely hot temperatures and neutron-rich environments ($T > 10^9$ K, $n_n > 10^{20}$ cm^{-3}) allow a rapid (r) nucleosynthesis process. In this process times between subsequent neutron capture events are much shorter than the time necessary for β decay, such that exotic nuclides can be produced. On the contrary, in the stellar evolution of asymptotic giant branch (AGB) stars, when the helium in the core is exhausted ($T \approx 10^8$ K, $n_n \approx 10^8$ cm^{-3}), a slow (s) process can take place. This process is expected to dominate for the production of Zr isotopes. In this case the average time between two neutron capture reactions is in the order of months or years and the reaction chain of subsequent neutron captures and β decays follows the valley of β stability. Given the progress made in astronomical observations and in models describing the stellar behavior, the understanding of nucleosynthesis processes strongly depends on the accuracy of the underlying neutron capture cross sections. The production of Zr isotopes is a typical example. These isotopes are predominantly of s-process origin and belong to the first s-process peak in the solar abundance distribution around mass number $A \approx 90$, where the proximity to the neutron magic number $N = 50$ causes a bottleneck in the reaction flow from Fe towards heavier elements. Additionally, Zr isotopes fall right in the matching region between the so-called weak s process (that takes place in massive stars) and the main s process (acting in AGB stars). Therefore, an accurate knowledge of their neutron capture cross section is of high interest.

A chemical analysis of stardust grains (specks of dust, extracted from primitive meteorites) has revealed isotopic compositions of many elements very different from those of the bulk of solar system material [4–6]. Isotopic anomalies are the signature of their formation in different astrophysical environments, from giant stars to novae and supernovae. Silicon carbide (SiC) grains have been the most extensively studied type of stardust. A comparison of AGB predictions to the Zr composition of SiC data presented disagreements [7]; in particular the ^{92}Zr / ^{94}Zr ratio was higher than predicted.

Providing improved neutron capture cross section data for Zr isotopes may be a key to solve this problem.

In the field of nuclear technology the transmutation of long-lived fission products (^{93}Zr among them) by neutron capture is relevant for a potential destruction of nuclear waste [8]. To assess the effectiveness of a transmutation scheme, cross sections for neutron interactions with the unstable ^{93}Zr isotope have to be combined with those for the stable isotopes, given that they are all produced by fission and that the transmutable waste will not be isotopically separated.

Only a limited number of cross section measurements for the ^{92}Zr(n, γ) reaction were carried out in the past [9–15]. Most of the information to evaluate resonance parameters and to subsequently derive Maxwellian averaged cross sections (MACSs) was obtained from the results of experiments carried out at ORELA [9] and n_TOF [15]. Some discrepancies are observed between these data. For example, the capture kernels for the strong resonances up to 8 keV differ up to a factor 3 (see Table III of Ref. [15]).

The parameters of Boldeman *et al.* [9] are the basis of the JENDL-2.0 evaluation in the resolved resonance region (RRR). These parameters were taken over in the ENDF/B-VII.0, JEFF-3.3, and JENDL-4.0 evaluated data libraries. In the ENDF/B-VIII.0 library some of the parameters, mainly radiative widths and spins, were changed based on the results of Ref. [15]. However, for some resonances the spin assignments were altered without maintaining the resonance strengths of Boldeman *et al.* [9]. Unfortunately, these changes are not documented. Furthermore, the parameters listed in Refs. [9,15] are adopted in the compilations of Mughabghab [16] and Sukhoruchkin and Soroko [17].

The MACS at 30 keV derived from the cross sections recommended in ENDF/B-VIII.0 (41.4 mb), JEFF-3.3 (44.6 mb), and JENDL-4.0 (40.5 mb) differ by more than one standard deviation from the value 37.8(30) mb recommended in the KADONIS database. Further, the MACS of 34(4) mb reported by Boldeman *et al.* [9][1] is in very good agreement with 34(6) mb of Macklin and Gibbons [11]. The latter was obtained from low resolution time-of-flight (TOF) measurements that were dedicated to derive MACS at an average energy of 30 keV. From the capture cross section of Ref. [15] the capture kernels for individual resonances were derived only up to an energy of 40 keV. Therefore, these data need to be complemented with results from evaluated data libraries to derive MACSs that can be used for stellar nucleosynthesis calculations.

To improve the status of the experimental data and to allow for a new evaluation, capture and transmission measurements at the GELINA facility of the JRC Geel (BE) were complemented with capture measurements at the n_TOF facility of CERN (CH). Bias effects due to sample properties were reduced by using metallic samples. The resulting transmissions and capture yields were combined in a resonance shape analysis to derive resonance parameters of individual resonances.

[1]A correction factor was later proposed by Allen, Boldeman, and Macklin [18] slightly changing the value to 33(4) mb.

The experimental details are described in Sec. II, the data reduction procedures in Sec. III, and the results of a resonance shape analysis in Sec. IV. A comparison with results of previous measurements is made in Sec. V. Section VI presents the results dealing with average resonance parameters and discussing the implications for the Maxwellian averaged cross sections. Finally, conclusions are drawn in Sec. VII.

II. EXPERIMENTAL DETAILS

A. Neutron capture measurements

Time-of-flight capture cross section measurements were performed at the n_TOF and GELINA facilities applying the total energy detection principle [19].

The experiments at the n_TOF facility were carried out at the experimental area 1 (EAR-1) [20,21]. Neutrons are produced in an energy range from thermal up to 1 GeV by spallation reactions in a massive lead block by proton bunches of high energy (20 GeV) and high intensity (7×10^{12} protons per bunch). With a conversion ratio of about 300 neutrons per proton, each proton pulse produces a neutron beam with an intensity of 10^5 neutrons/cm^2 per pulse in EAR-1, which is placed 185 m from the spallation target. Thanks to both the long flight path and the short proton pulse width of 7 ns a high neutron energy resolution is achieved (see, e.g., Table 3 of Ref. [20]).

The lead spallation target is connected with EAR-1 by an evacuated beam line. Charged particles are removed from the neutron beam by a 1.5 T sweeping magnet. Neutrons and ultrarelativistic particles outside the beam line are suppressed by heavy concrete walls and a massive iron shielding 3.5 m in thickness. The neutron beam is shaped by two collimators, the second one placed close to the last shielding wall upstream of the experimental area. The 18 mm aperture of the second collimator produces a nearly symmetric Gaussian-shaped beam profile with a width of 2 cm at the sample position [20]. The sample position was fixed at 185.2 m from the spallation source. The beam line extends 12 m beyond EAR-1 to minimize the effect of backscattered neutrons.

The energy distribution of the incident neutron beam was determined based on the ^{235}U(n, f) reaction using a calibrated fission chamber from Physikalisch Technische Bundensanstalt Braunschweig [22]. The neutron beam intensity was checked online during the capture measurements by a low-mass ^{6}Li neutron monitor, consisting of a ^{6}Li deposit on a Mylar foil and four off-beam silicon detectors measuring the charged particles emitted in the ^{6}Li(n, α) ^{3}H reaction [23].

Additional capture cross section measurements were performed at the time-of-flight facility GELINA of the JRC Geel (BE). A detailed description of this facility can be found in Ref. [24]. Intense pulsed electron beams are accelerated to a maximum energy of 150 MeV at a repetition rate of 400 Hz. The pulsed electron bunches are compressed to a duration of less than 2 ns by a post-acceleration compression magnet [25]. High-energy electrons generate Bremsstrahlung in a mercury-cooled rotating uranium target, where neutrons are produced by (γ, n) and (γ, f) reactions [26]. To produce a neutron spectrum in the low energy region, two water-filled beryllium containers 4 cm in thickness are used as moderators.

A shielding made of Cu and Pb is placed close to the uranium target to reduce the intensity of the γ-ray flash and the fast neutron component. The BF_3 proportional counters, placed at different locations around the target hall, are used to monitor the stability of the accelerator and to normalize TOF spectra to the same total neutron intensity. All measurement stations are equipped with an air-conditioning system to keep the sample at a temperature of 22 °C and to avoid electronic drifts due to temperature changes. The temperature in the stations is continuously monitored.

The capture measurements at GELINA were performed at a 30-m station of a flight path that forms an angle of 0° with respect to the normal of the moderator facet viewing the flight path. The sample was positioned at 28.82 m from the center of the moderator. The moderated neutron beam was collimated to 75 mm in diameter at the sample position. A ^{10}B antioverlap filter was placed in the beam to absorb slow neutrons from a previous burst. To monitor the background the measurements were done with at least one fixed black resonance filter (S and/or Na) in the beam. The measurements with only the S filter in the beam were carried out to determine the resonance parameters of the 2.68 keV resonance. The energy distribution of the incident neutron beam was measured simultaneously with a Frisch gridded ionization chamber placed at 80 cm before the sample. The chamber was operated with a continuous flow of a mixture of argon (90%) and methane (10%) at atmospheric pressure. The detector consisted of two ionization chambers with a common cathode loaded with two layers of ^{10}B. The ^{10}B layers, with an effective diameter of 84 mm and areal density of about 40 μg/cm^2, were evaporated back to back on a 30-μm-thick aluminium backing and the entrance and exit windows of the chamber had a thickness of 40 μm.

The capture detection systems at the n_TOF and GELINA facilities consisted of a pair of C_6D_6-based liquid scintillators. Each detector was positioned at an angle of 125° with respect to the direction of the neutron beam. This geometry minimizes systematic effects due to the anisotropy in the primary γ-ray emission. Deuterated benzene (C_6D_6) was chosen for its very small neutron sensitivity, given that deuterium and carbon have very low neutron capture cross sections. The detection probability of scattered neutrons was further reduced by coupling each scintillator to a boron-free quartz windowed photomultiplier.

The total energy detection principle [19] was used by combining the detection systems described above with the pulse height weighting technique. When applying this technique the efficiency of detecting a γ-ray becomes directly proportional to its energy. This technique is based on a suggestion by Maier-Leibnitz and was first applied by Macklin and Gibson [27] using C_6F_6 detectors. The weighting functions were derived by Monte Carlo simulations based on the work of Ref. [28]. In the calculation of the weighting function the effect of γ-ray attenuation in the sample and the discrimination level of the detection system was taken into account.

B. Transmission measurements

The transmission experiments were performed at a 25-m station of the GELINA facility using the moderated neutron beam. A description of this station can be found in Refs. [29,30]. The accelerator was operated at a 800 Hz frequency. The flight path forms an angle of 9° with the direction normal to the facet of the moderator viewing the flight path.

The neutron beam was collimated to a diameter of 15 mm at the sample position. The samples were placed at 9 m distance from the neutron source. Close to the sample position a ^{10}B antioverlap filter was placed in the beam to absorb slow neutrons from a previous burst. The impact of the γ-ray flash was reduced by a 5-mm-thick Pb filter. Permanent black resonance filters (Co and Na) were used to reduce bias effects related to background corrections. The neutron beam passing through the sample and filters was further collimated and detected by a 12.7-mm-thick and 101-mm-diameter NE905 Li-glass scintillator enriched to 95% in ^{6}Li. The scintillator was connected through a boron-free quartz window to an EMI-9823 KQB photomultiplier. The detector was placed at 24.5 m from the neutron-producing target.

TABLE I. Isotopic composition of the samples (in atom %).

^{90}Zr	^{91}Zr	^{92}Zr	^{94}Zr	^{96}Zr
2.50(2)	1.11(1)	95.17(3)	1.09(1)	0.13(1)

C. Samples

Highly enriched ^{92}Zr samples, delivered by the Oak Ridge National Laboratory, were used to perform the transmission and capture cross section measurements. To avoid bias effects due to a possible grain size distribution of powder samples (see, e.g., Refs. [19,31]), measurements were carried out with metallic samples. The isotopic composition of the ^{92}Zr samples is summarized in Table I. The samples were of cylindrical shape with a diameter of 2 cm. Three different samples were used with a mass of 1.954, 4.960, and 9.991 g. For the capture measurements only the thinner and the thicker ones were used. Transmission data were obtained with three samples with weights of 1.954, 9.991, and 16.905 g. The last one was made by stacking all three samples.

To derive the capture yields normalization measurements were performed. At the n_TOF facility a 1-mm-thick metallic Au sample was used. The normalization at the GELINA facility was based on results from measurements with a 4-mm-thick metallic natural Fe sample. The Au and Fe samples used for the normalization measurements were discs with the same diameter as the ^{92}Zr samples. The background contributions were estimated from results of capture measurements with a natural carbon sample.

III. DATA REDUCTION

A. Capture

The experimental capture yield $Y_{\rm exp}(t)$ as a function of time of flight t was deduced from the weighted response of the C_6D_6 scintillators created by prompt γ rays emitted after a neutron capture reaction in the sample and the energy distribution of the incident neutron beam φ:

$$Y_{\rm exp}(t) = \frac{N_c}{S_n + E_n(t)\frac{m_{Zr}}{m_n+m_{Zr}}}\frac{C_w(t) - B_w(t)}{\varphi(t)}, \qquad (1)$$

where C_w is the dead time corrected weighted response, B_w the corresponding background contribution, E_n is the kinetic energy of the incident neutron, S_n is the neutron separation energy and N_c is a normalization factor. The atomic mass of the neutron and target nucleus are denoted by m_n and m_{Zr}, respectively.

The background contribution $B_w(t)$ of the C_6D_6 detectors was expressed as [19]:

$$B_w(t) = b_0 + C_{w,0}(t) + R_n(t)(C_{w,C}(t) - C_{w,0}(t)), \quad (2)$$

where b_0 is a time-independent contribution, $C_{w,0}(t)$ and $C_{w,C}(t)$ are the weighted TOF spectra from measurements with no sample and with an almost purely scattering natural carbon sample, respectively. The spectra $C_{w,0}(t)$ and $C_{w,C}(t)$ were obtained using the weighting function calculated for the ^{92}Zr sample. They were normalized to the same integrated neutron intensity and corrected for the time independent background beforehand. The correction factor $R_n(t)$ is the ratio of the neutron scattering yield of the Zr and C sample. This correction was derived iteratively by calculations with the code REFIT [32].

The normalization factor N_c in Eq. (1) accounts for TOF independent quantities such as the absolute intensity of the incident neutron beam, the effective sample area seen by the neutron beam, the absolute detection efficiency, and the solid angle subtended by the sample and the C_6D_6 detectors. For the n_TOF data this factor was derived from an analysis of the saturated resonance profile of the 4.9 eV resonance resulting from normalization measurements with a Au sample, for details see [33,34]. The resonance parameters reported in Ref. [35] were used. It should be noted that by restricting the analysis to the top of the resonance profile the normalization is almost independent of the parameters and areal density of the Au sample as demonstrated in Ref. [28]. The capture data from the measurements at GELINA were normalized based on a resonance shape analysis of the capture yield around the 1.15 keV resonance of ^{56}Fe obtained from the measurement with a natural Fe sample. The neutron width $\Gamma_n = 61.7(9)$ meV and radiative width $\Gamma_\gamma = 574(40)$ meV for this analysis were taken from Ref. [36]. The uncertainty of the normalization factor applying this procedure is less than 2% as demonstrated in Refs. [28,37].

B. Transmission

The experimental transmission $T_{\rm exp}(t)$ was derived from the ratio of a sample-in spectrum, $C_{\rm in}(t)$, and a sample-out spectrum, $C_{\rm out}(t)$, after correcting for their background contributions $B_{\rm in}(t)$ and $B_{\rm out}(t)$, respectively:

$$T_{\rm exp}(t) = N_t \frac{C_{\rm in}(t) - B_{\rm in}(t)}{C_{\rm out}(t) - B_{\rm out}(t)}. \quad (3)$$

The spectra ($C_{\rm in}$ and $C_{\rm out}$) in Eq. (3) were corrected for losses due to dead time. All spectra were normalized to the same neutron intensity. The normalization factor N_t accounts for the ratio of the integrated intensities of the incident neutron beam during the sample-in and sample-out cycles of the sample. This factor was obtained using the signals from the BF_3 neutron monitors. To reduce systematic effects due to slow variations of both the beam intensity and detector efficiency as a function of time, data were taken by alternating sample-in and sample-out measurements in cycles of about 15 minutes each. Such a procedure reduces the uncertainty on the normalization factor N_t to less than 0.25% [19].

The background as a function of TOF was parameterized by an analytical expression consisting of a constant and three exponentials [30]:

$$B(t) = a_0 + a_1 e^{-\lambda_1 t} + a_2 e^{-\lambda_2 t} + a_3 e^{-\lambda_3 (t+\tau_0)}. \quad (4)$$

The first exponential is due to the detection of 2.2 MeV γ rays from neutron capture in hydrogen present in the moderator. The second exponential originates predominantly from neutrons scattered inside the detector station. The third one is due to slow neutrons from previous accelerator cycles; τ_0 is related to the frequency of the accelerator (2.5 ms in the present case, corresponding to the accelerator frequency of 400 Hz). The free parameters in the analytical expression were determined by a least-squares fit to saturated resonance dips observed in the TOF-spectra resulting from measurements with black resonance filters. During the regular sample-in and sample-out runs at least one black resonance filter (Co and/or Na) was kept in the beam to account for the dependence of the background level on the presence of the sample [19].

IV. RESULTS OF A RESONANCE SHAPE ANALYSIS

Resonance parameters (see Table II) were derived from a resonance shape analysis of the experimental data based on the Reich-Moore approximation [38] of the $\mathcal{R}$-matrix formalism [39]. The REFIT [32] and SAMMY [40] codes were used to analyze the GELINA and n_TOF data, respectively.

These codes account for various experimental effects such as Doppler broadening, neutron self-shielding and multiple interaction events, the detection efficiency of the capture detector, sample properties, the response function of both the TOF-spectrometer and neutron detector for transmission measurements, as well as for the impurities of the samples, i.e., contamination of other Zr isotopes. The capture yields derived at n_TOF were analyzed using analytical response functions based on Ref. [20]. To analyze the data obtained at GELINA numerical response functions reported in Ref. [41] were used. For the analysis of the transmission data these response functions were folded with analytical expressions to account for the time response of the Li-glass scintillator (see, e.g., [19]). The REFIT code was used due to its flexibility to combine different TOF-response functions, both numerical and analytical, accounting for the time response of the pulsed charged particle beam, neutron transport in the moderator, and time response of the detector. It also includes a module to calculate the TOF response functions of a neutron detector based on the design properties and material composition of the detector.

The initial resonance parameters, including an effective scattering radius of $R' = 7.2$ fm and one negative resonance, were taken from JENDL [42]. These parameters are based on those compiled by Mughabghab [16]. The analysis was done without including an additional background cross section. Therefore, the contribution of the negative resonance accounts

TABLE II. Resonances parameters for neutron interactions with ^{92}Zr derived from a simultaneous analysis of capture and transmission data with REFIT. The quoted uncertainties are only due to propagating uncorrelated uncertainties due to counting statistics. The parameters of the negative resonance included in the analysis are also given. For resonances marked with a dagger (†) J^{π} is uncertain due to small significance of the differences in fits for various J^{π}. Resonances for which the spin and/or parity were changed compared to the assignments by Boldeman *et al.* [9] are marked with a cross (×). In the case of a presence of multiplet structure the kernel was directly extracted from the capture resonance area.

E_R (eV)	Γ_γ (eV)	Γ_n (eV)	J	ℓ	K (eV)	$\frac{\Delta K}{K}$ (%)
−1350.00	0.118	29.0	1/2	0		
2011.25(9)	0.44(2)	0.0273(1)	3/2	1	0.0514	7.8
2684.66(7)	0.056(1)	24.78(4)	1/2	0	0.0554	2.3
4116.29(7)	0.208(3)	3.44(2)	3/2	1	0.392	2.0
4634.00(9)	0.062(2)	14.58(6)	1/2	0	0.0621	3.2
5039.9(2)	0.191(3)	1.23(3)	1/2	1	0.165	3.8
6632.2(3)	0.292(4)	1.28(3)	3/2	1	0.475	3.7
6794.6(2)	0.229(4)	73.4(2)	1/2	0	0.228	2.1
8835.7(3)	0.096(2)	3.71(8)	1/2	1	0.0935	4.4 †
9127.3(3)	0.067(2)	5.22(8)	1/2	0	0.0665	4.0
9815.9(2)	0.112(2)	1.67(6)	3/2	1	0.209	5.5 †
11935.7(5)	0.153(3)	2.3(1)	3/2	1	0.287	5.6
12005.4(4)	0.146(4)	8.3(2)	1/2	1	0.144	4.3 †
13059.8(7)	0.121(4)	2.1(1)	3/2	1	0.229	7.9
14414.2(6)	0.152(4)	12.6(2)	1/2	1	0.150	4.3 †
15021(3)				1	0.109	17 †
17116.1(7)	0.121(3)	11.0(2)	3/2	1	0.238	4.0
19064(3)	0.171(4)	2.7(2)	3/2	1	0.323	8.9
20188(9)	0.29(1)	1.0(3)	1/2	1	0.23	30 ×
20847(3)			1/2	1	0.34	14 †
21966(6)			1/2	1	0.28	16 †
23080.8(6)			1/2	0	0.11	18 †
25107(2)					0.033	51
25675(6)			1/2	1	0.097	18 †, ×
26765(9)			1/2	1	0.20	27 †
27322(1)	0.301(8)	18.2(6)	1/2	1	0.296	5.6 †
28071(3)			3/2	1	0.17	15.8
28149(2)	0.25(1)	18.2(6)	1/2	1	0.243	8.6
30361(7)					0.15	20
30922(3)	0.25(1)	11.4(5)	3/2	1	0.489	6.8 †
32468(5)	0.210(6)	9.7(6)	3/2	1	0.412	8.7 †
33098(7)			1/2	0	0.13	15 †
35031(4)	0.17(8)	49(2)	1/2	1	0.165	8.7 †
35670(3)	0.277(9)	52(2)	1/2	1	0.275	6.9
35939(4)				1	0.351	7.6
37536(16)				1	0.30	21 †
38737(2)			1/2	1	0.11	86 †
38931(2)	0.229(7)	6.0(7)	3/2	1	0.44	16
39326(4)			1/2	1	0.297	7.9 †
39479(4)			1/2	0	0.06	22 †
41225(14)			3/2	1	0.328	20 †
43759(2)			1/2	1	0.324	23 †
45079(3)	0.30(1)	82(2)	1/2	1	0.301	5.8 †
45754(3)	0.29(1)	28(1)	1/2	1	0.291	8.9 †
≈46900					1.04	2.1 Multiplet
47667(4)			1/2	0	0.202	8.6 †
47862(8)			3/2	1	0.19	25 †
49337(3)			1/2	1	0.30	11 †
49807(2)			3/2	1	0.60	25 †
52695(3)	0.173(9)	117(2)	1/2	0	0.172	7.2 †
53559(4)	0.31(1)	18(2)	1/2	1	0.31	13
54513(2)			1/2	1	0.361	4.3 †
55779(13)					0.09	90
56222(5)			1/2	0	0.18	12 †
56525(3)			3/2	1	0.46	16 †
58188(6)			1/2	1	0.20	16 †
58647(9)					0.159	7.4
59056(7)					0.135	9.0
60642(6)			3/2	1	0.16	50 †
61036(4)	0.21(1)	64(2)	3/2	1	0.417	6.3 †
62003(4)			3/2	1	0.26	59 †
62693(7)			1/2	1	0.19	15 †
63477(3)	0.33(1)	57(2)	3/2	1	0.648	5.9 †
65031(9)					0.128	8.4
65300(6)					0.283	6.2
65545(5)					0.2	46
67504(4)			3/2	1	0.42	29 †
≈ 69200					0.59	10 Doublet
69343(5)					0.214	7.4
72365(6)					0.254	8.0
72838(6)					0.350	6.0
73807(7)					0.22	25
76134(6)					0.36	10
77025(2)					0.308	5.9
80811(10)					0.378	5.3

also for a possible direct radiative capture (DRC) component. As there are very few negative-parity states at low excitation energy in ^{93}Zr, DRC due to *s*-wave neutrons is unlikely to take place. Theoretical calculations based on a Wood-Saxon type potential show that the contribution of *p*-wave DRC becomes only significant for neutron energies above 100 keV [43].

The REFIT code was used to determine the resonance parameters by a simultaneous least-squares adjustment to the transmissions and capture yields resulting from the GELINA measurements in the energy region below 81 keV. The free gas model, with an effective temperature of $T_{\rm eff} = 300$ K, was applied to account for the Doppler effect. The flight path distance of the capture setup was adjusted in a simultaneous analysis with the transmission data fixing the flight path distance for the transmission data to $L = 24.328(4)$ m. This distance was derived from previous transmission measurements with an uranium sample at the same measurement station of GELINA using the parameters recommended by Derrien *et al.* [44]. Hence, the resonance energies reported in this work are relative to those reported by Derrien *et al.* [44], which were derived from an analysis of a series of transmission measurements performed at ORELA. In cases when the experimental data were not good enough to determine both the neutron and radiative width, the data were fitted using

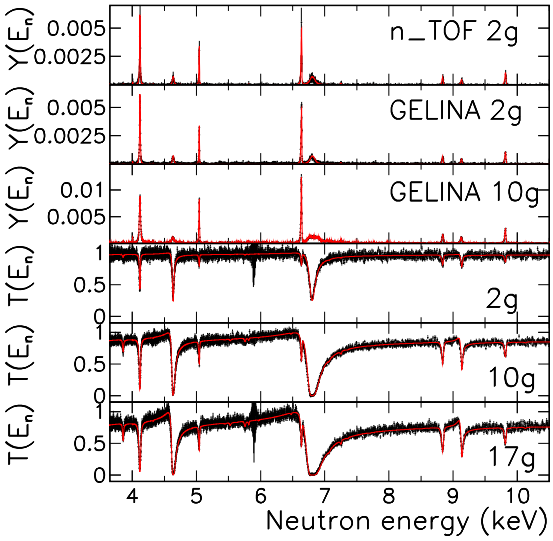

FIG. 1. Comparison of the experimental (black) and theoretical (red) capture yields and transmissions. The theoretical data are the result of a least squares adjustment to the GELINA data set with REFIT. The capture yield for the n_TOF data was calculated with SAMMY using these parameters. Upper panels: capture yields obtained at n_TOF and GELINA with the 2 and 10 g ^{92}Zr samples. Lower panels: transmissions obtained at GELINA with the 2, 10, and 17 g ^{92}Zr samples.

a fixed neutron width defined by the initial parameters. For these resonances only the capture kernel is reported. Results of a least-squares adjustment to the data with REFIT are shown in Figs. 1–3. The orbital momentum was unambiguously determined for strong s-wave resonances. The identification was based on the characteristic resonance interference profile of s-wave resonances in the transmission data (e.g., the s-wave

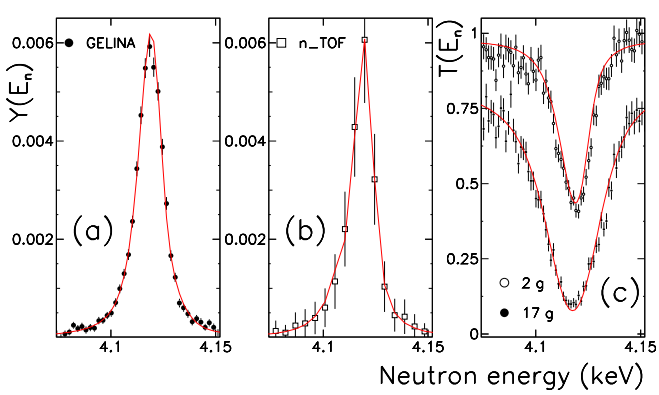

FIG. 2. Capture yields and transmissions in the energy region of the 4116 eV resonance. The experimental capture yields in panels (a) and (b) are obtained from measurements with a 2 g ^{92}Zr sample at GELINA and n_TOF, respectively. The experimental transmissions in panel (c) result from measurements at GELINA with the 2 and 17 g ^{92}Zr samples. The experimental data are compared with the calculated capture yields and transmissions using the parameters resulting from a least-squares adjustment only to the GELINA data using REFIT. The theoretical capture yield for the n_TOF data in panel (b) was calculated with SAMMY.

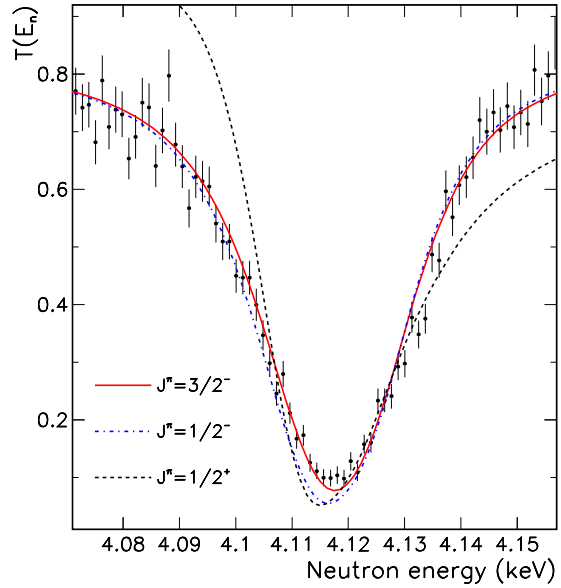

FIG. 3. Transmission through the 17 g ^{92}Zr sample around the 4116 eV resonance. The experimental transmission (full dots) is compared with the theoretical ones supposing $J^\pi = 1/2^+$, $1/2^-$, and $3/2^-$.

resonances at 4634, 6795, and 9127 eV in Fig. 1). Transmission data also allowed to assign the spin of several p-wave resonances. This is illustrated in Fig. 3, where experimental data for the 4116 eV resonance are compared with the calculated resonance profiles supposing $J^\pi = 1/2^+$, $1/2^-$, and $3/2^-$. The data give clear preference to $3/2^-$ assignment for this resonance.

The parameters derived from a fit to the GELINA data were verified by comparing the experimental capture yield derived from the n_TOF data to the calculated yield using these parameters. Due to limitation in the counting statistics of the n_TOF data this verification was only done for energies below 40 keV. An example of such a verification is given in Fig. 2.

The n_TOF data were also used to determine the capture kernels for resonances with an energy below 40 keV from a least-squares adjustment with SAMMY. The neutron widths were fixed to those derived from the fit to the GELINA data. The average ratio of the kernels extracted from the n_TOF data and GELINA data is 1.006, with a standard deviation of 0.031.

The full procedure, i.e., fit to GELINA data and verification by n_TOF data, was applied without any additional background or normalization correction to the GELINA or n_TOF data. This shows that the transmission and capture yields, which were derived in this work from experiments at two TOF facilities with different response functions, background conditions, and normalization procedures, can be parametrized by using one set of resonance parameters.

A few resonances with high values of both Γ_n and Γ_γ ($\Gamma_\gamma \gtrsim 0.5$ eV) are listed in Ref. [9]; therein they play an important role in a discussion of a possible valence neutron capture contribution. The only resonance of this kind below 81 keV, i.e., the upper limit of the present measurement, was

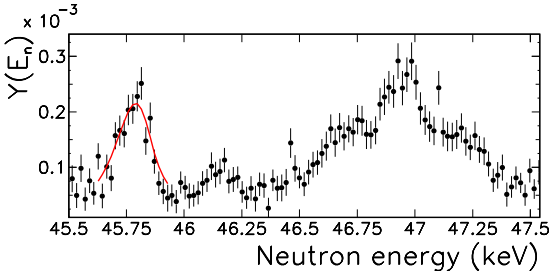

FIG. 4. Experimental capture yield (full dots) for the 10 g ^{92}Zr sample around the 46.9 keV resonance measured at GELINA. The theoretical data (red line) around the 45.7 keV resonance are the result of a least-squares adjustment of the data set with REFIT.

located near 47 keV. The capture data obtained at GELINA suggest the presence of a multiplet structure in this region; see Fig. 4. Unfortunately, we were not able to unambiguously disentangle the structure into individual resonances. Nevertheless, this example indicates that the parameters of individual resonances at higher neutron energies should be taken with care as some of the strong resonances could in reality be multiplets. The impact of valence neutron capture can thus be questionable and better quality data at higher energies are needed before drawing conclusions.

In total, parameters for 74 resonances[2] were determined in the energy region below 81 keV. Resonances at 16.94, 17.28, 26.23, and 28.28 keV, listed in Ref. [15], were not confirmed by the present analysis. The weak resonance at 39.66 keV, that was reported in Ref. [9], was not observed. The list of resonance given in this publication is not complete. We only list the resonances for which we could determine at least some resonance parameters with sufficient accuracy using only the presented experimental data sets. These resonance parameters are listed in Table III including the capture kernel K_γ defined as

$$K_\gamma = g\frac{\Gamma_n\Gamma_\gamma}{(\Gamma_n+\Gamma_\gamma)}, \tag{5}$$

where

$$g = \frac{(2J+1)}{2(2I+1)} \tag{6}$$

is the statistical spin factor determined by the resonance spin J and the spin of the target nucleus $I = 0$.

For several resonances it was not possible to extract the Γ_n, Γ_γ, J, and ℓ with sufficient confidence, hence only the capture kernels are reported for these cases. The quoted uncertainties result from propagating only uncorrelated uncertainties due to counting statistics. For a final uncertainty evaluation the uncertainty of correlated components such as the normalization of the capture data has to be included. This uncertainty is about 4% [45] and 2% [28] for the n_TOF and GELINA data, respectively.

Resonance parameters determined in this work account for about 15% of the capture cross section of 250(75) mb at thermal energy measured by Pomerance [46]. This value, coming from pile oscillator measurements, is the only experimental value that is reported in the literature. The small contribution

[2]In reality, our data strongly suggest that two of these are multiplets; see Table III.

TABLE III. Total MACS together with different contributions for kT from 5 to 100 keV. The contribution from the capture kernels of observed resonances plus $1/v$ component normalized to 37 mb plus the negative resonance, and DRC are given. The contributions for energies above 81 keV are calculated from cross section data in the ENDF/B-VIII.0, JEFF-3.3, and JENDL-4.0 libraries. The total MACS derived from the sum of experimental data complemented with the contribution obtained from the ENDF/B-VIII.0 library is presented in the last column.

kT (keV)	Kernels + $1/v$ + negative resonance (mb)	DRC (mb)	JENDL-4.0 (mb)	ENDF/B-VIII $E_n > 81$ keV (mb)	JEFF 3.3 (mb)	Total MACS full range (mb)
5	127.4 (65)	0.41	$\approx 10^{-2}$	$\approx 10^{-2}$	$\approx 10^{-2}$	127.8 (65)
8	92.7 (47)	0.58	$\approx 10^{-2}$	$\approx 10^{-2}$	$\approx 10^{-2}$	93.3 (47)
10	78.5 (40)	0.68	0.1	0.1	0.1	79.2 (40)
15	57.2 (29)	0.93	0.5	0.8	1.2	58.9 (29)
20	44.8 (23)	1.15	1.5	2.3	3.1	48.2 (23)
23	39.4 (20)	1.28	2.3	3.4	4.4	44.1 (21)
25	36.4 (18)	1.36	2.9	4.3	5.2	42.0 (20)
30	30.1 (15)	1.56	4.2	6.4	7.0	38.1 (18)
35	25.4 (13)	1.75	5.5	8.4	8.4	35.5 (18)
40	21.6 (11)	1.93	6.6	10.3	9.6	33.9 (19)
45	18.7 (10)	2.11	7.6	12.0	10.4	32.8 (21)
50	16.3 (8)	2.28	8.4	13.5	11.1	32.0 (22)
55	14.3 (7)	2.45	9.1	14.8	11.7	31.6 (24)
60	12.6 (7)	2.62	9.7	16.0	12.1	31.3 (25)
70	10.1 (5)	2.94	10.6	17.9	12.8	31.0 (28)
80	8.2 (4)	3.25	11.2	19.4	13.3	30.9 (30)
90	6.8 (4)	3.55	11.7	20.6	13.7	31.0 (32)
100	5.8 (3)	3.84	12.0	21.5	13.9	31.2 (33)

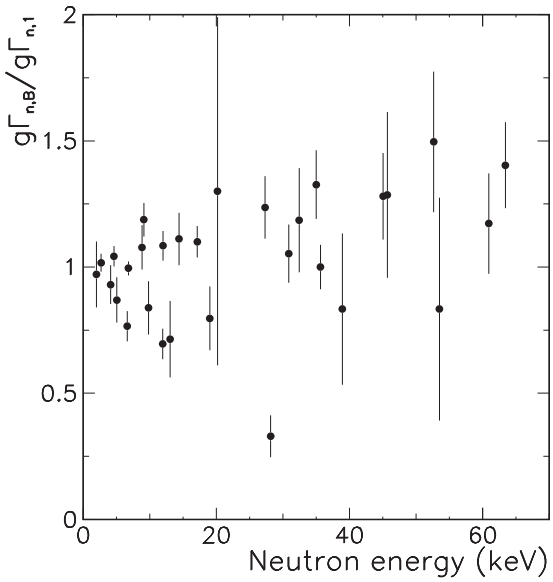

FIG. 5. Ratio of the resonance strength $g\Gamma_{n,B}$ derived by Boldeman *et al.* [9] and the one obtained in this work $g\Gamma_{n,1}$ as a function of neutron energy.

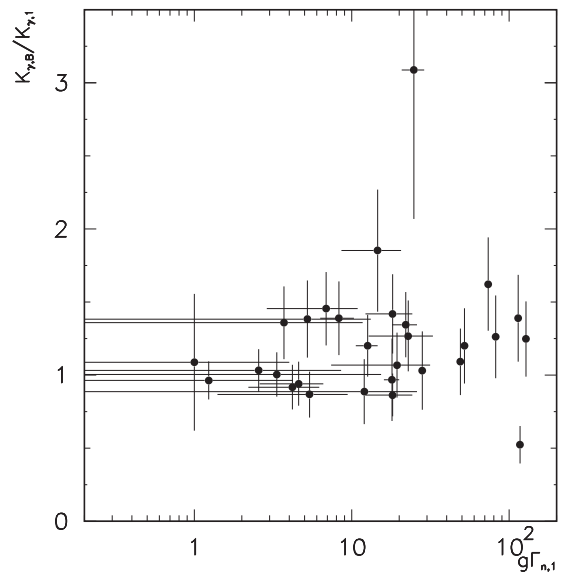

FIG. 6. Ratio of the capture kernel $K_{\gamma,B}$ derived by Boldeman *et al.* [9] and the one obtained in this work $K_{\gamma,1}$ as a function of the resonance strength $g\Gamma_n$.

of 37 mb by observed resonances and low probability of a DRC component indicates a significant contribution of a negative resonance. This explains the need of a bound state. Its parameters are included in Table III. The coherent scattering length $b_c = 7.58$ fm derived from the resonance parameters is consistent with the length $b_c = 7.5(2)$ fm measured by Koester *et al.* [47].

V. COMPARISON WITH RESULTS FROM PREVIOUS MEASUREMENTS

Parameters of individual resonances derived from experimental data were previously reported in Refs. [9,15]. Boldeman *et al.* [9] performed capture cross section measurements using a pair of C_6F_6 liquid scintillators [48] and transmission measurements using a ^{6}Li glass scintillator at ORELA. They derived parameters of resonances in the energy region up to 120 keV.

The ratio of $g\Gamma_n$ derived from the parameters of Boldeman *et al.* [9] and from those reported in this work is shown in Fig. 5 as a function of the incident neutron energy. The average ratio is 1.03. There is an indication of a systematic increase of the ratio with increasing energy. The strong variation of the ratio between 0.3 and 1.5 for individual resonances is most likely due to the difference in codes that were used for the analysis. Unfortunately, no detailed information about the analysis procedure is given in Ref. [9]. It seems that a kind of resonance shape analysis was applied based on a single level Breit-Wigner approximation. No details about including the experimental effects, such as the TOF-response functions, are given.

The ratio of the kernels derived from the parameters of Boldeman *et al.* [9] and those obtained in this work are plotted as a function of $g\Gamma_n$ in Fig. 6. The weighted average ratio is 1.04 and no clear dependence on resonance strength is observed. This suggests that the data of Boldeman *et al.* [9] are properly corrected for the neutron sensitivity of the detection system. A small difference could be due to an error in the computer code used for the data reduction as reported in Ref. [18]; in particular, an overall correction factor of 0.9833 is required for the experimental capture yields of ^{92}Zr in Ref. [9] due to this error and considering the discussion in Ref. [18] a new resonance shape analysis of the data presented in Ref. [9] would be required to properly correct for the error, especially in case of self-shielding effects.

The data of Ref. [15] were derived from capture cross section measurements at the n_TOF facility using C_6D_6 detectors. Figure 7 compares the capture kernels derived in this work with those of Ref. [15], by plotting the residuals as a function of neutron energy. The residuals are defined as

$$R = \frac{K_{\gamma,2} - K_{\gamma,1}}{u_K}, \tag{7}$$

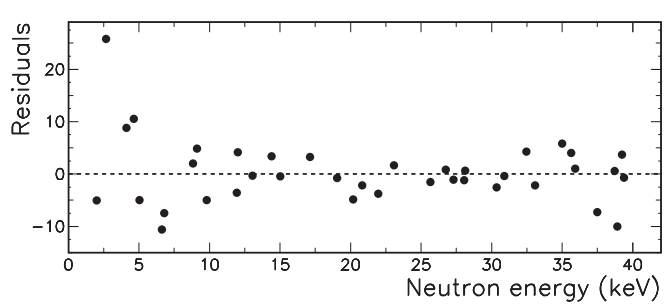

FIG. 7. Comparison of kernels from present and previous [15] n_TOF measurement by plotting the residuals (defined in the text) as a function of neutron energy.

where $K_{\gamma,2}$ and $K_{\gamma,1}$ are the capture kernels obtained in Ref. [15] and in this work, respectively, and u_K is the combined uncertainty of the difference. For resonances with an energy below 8 keV substantial differences are observed. For energies above 8 keV the average is close to zero, but with a standard deviation of about 2.7.

Main differences between the present data and results from the previous capture cross section measurements at n_TOF [15] are related to the data reduction, analysis procedures and the sample properties. In Ref. [15] a yield was derived by dividing weighted counts—not corrected for any background contribution—by an energy distribution of the incident neutron beam φ based on an analytical expression adjusted to results of Monte Carlo simulations. Background corrections were applied as a part of the resonance shape analysis. This could lead to bias effects, in particular in the case of broad and overlapping resonance profiles, and an underestimation of the uncertainties due to background contributions. Such an underestimation could explain why the distribution of residuals for energies above 8 keV is wider than expected.

The present capture yields from GELINA and n_TOF are obtained by accounting for the background contributions including the one due to neutron scattering in the sample. They were used in the analysis procedure together with the transmission data without the need of introducing any additional background correction. Moreover, the analytical expression of φ used in Ref. [15] does not fully reproduce the dips that are observed in the experimental distribution, which leads to an underestimation of the capture yield in the regions where such dips occur. Other reasons to explain the differences in kernels can be the presence of impurities of the sample in Ref. [15] (i.e., 0.17 wt % of natural Hf) and the impact of the grain size distribution of the powder sample.

The present resonance parameters are obtained by combining transmission data and capture yields obtained at two different neutron TOF facilities under different background and normalization conditions. Therefore, it is expected that this will reduce some of the above mentioned systematic effects.

VI. AVERAGE RESONANCE PARAMETERS AND MAXWELLIAN AVERAGED CROSS SECTIONS

A. Average resonance parameters

The parameters of individual resonances in Table III were used to determine average resonance parameters.

To allow reproducibility of the results and considering a presence of a complicated multiplet structure near 47 keV, for which we had problems properly fitting the parameters, we decided to calculate neutron strength functions only based on resonances with energy below 46 keV. Missing neutron widths in Table III were complemented by those of Boldeman *et al.* [9] and a channel radius of 7 fm was considered for p-wave resonances. This resulted in $S_0 = 0.63(28) \times 10^{-4}$ and $S_1 = 5.2(13) \times 10^{-4}$ strength functions for s and p waves, respectively. The quoted uncertainties are derived from the expected Porter-Thomas fluctuations of reduced neutron widths assuming the resonance spacing determined below. The impact of the experimental uncertainties is small compared to the Porter-Thomas fluctuations.

The S_0 derived in this work is within uncertainties consistent with $S_0 = 0.76(28) \times 10^{-4}$ derived by Boldeman *et al.* [9], and $S_0 = 0.5(1) \times 10^{-4}$ from Ref. [16]. Values of $S_1 = 8.3(14) \times 10^{-4}$ and $S_1 = 7.0(13) \times 10^{-4}$ reported by Boldeman *et al.* [9] and Mughabghab [16], respectively, are higher than the one derived in this work. The difference is most probably due to the use of a different channel radius ($R = 6.06$ fm in [9]) and the influence of p-wave resonances at higher energies, a few of them being very strong in [9]; see also Fig. 5.

The average radiative width of s-wave resonances is $\overline{\Gamma}_\gamma^{(0)} = 95(10)$ meV. The standard deviation characterizing the width of the distribution is $s_{\Gamma_\gamma^{(0)}} = 32$ meV. The analogous quantities derived from the p-wave resonances with a firm spin assignment and $\Gamma_n > 10\,\Gamma_\gamma$ (the capture area is $\sim g\Gamma_\gamma$ in such a case) are $\overline{\Gamma}_\gamma^{(1)} = 176(35)$ meV and $s_{\Gamma_\gamma^{(1)}} = 64$ meV. The derived $\overline{\Gamma}_\gamma^{(0)}$ is consistent with 111(29) meV quoted by Mughabghab [16]. On the other hand, $\overline{\Gamma}_\gamma^{(1)}$ is significantly smaller than the value 319(34) meV of Ref. [16]. The difference for p-wave resonances comes from a presence of a few high Γ_γ ($\gtrsim$500 meV) values reported in [9] and adopted in [16]. The first of these values was assigned to a resonance structure near 46.9 keV, which we identified as a multiplet from our data; see Fig. 4. The actual radiative widths of individual resonances in this multiplet are definitely smaller than the single value given in Ref. [9]. A similar effect might be responsible for other high Γ_γ reported at higher neutron energies in [9].

The larger $\overline{\Gamma}_\gamma$ for p-wave (compared to s-wave) resonances can be explained by a contribution of strong primary $E1$ transitions to low lying positive-parity states in ^{93}Zr. A higher intensity of these primary transitions from p-wave resonances (with respect to thermal neutron capture) was observed by Kenny *et al.* [49] using 2 and 24 keV filtered neutron beams.

To derive the average resonance spacing taking into account the contribution of missing resonances a method similar to the one used in [50] was applied: the number of experimentally determined capture kernels and theoretical estimated ones above a given threshold were compared. The theoretical kernels were derived from statistical model calculations using the strength functions and average radiative widths discussed above. The spin dependence of the level density was assumed in the standard form yielding $D_0 \approx 2.85 D_1$; no parity dependence was considered. These assumptions are fully consistent with the present data. Data below 46 keV yield $D_0 = 4000(500)$ eV (with a very weak dependence on adopted channel radius); the maximum considered energy was limited by the complex structure at 46.9 keV. This value nicely agrees with 3800(510) eV in Ref. [16].

The determination of orbital angular momentum ℓ of a resonance is often based on a method originally developed by Bollinger and Thomas [51]. Details on this procedure can be found in, e.g., Refs. [52,53] and references therein. The method relies on a statistical analysis of individual reduced neutron widths, which are expected to follow a Porter-Thomas distribution [54] around the expectation value. It requires the

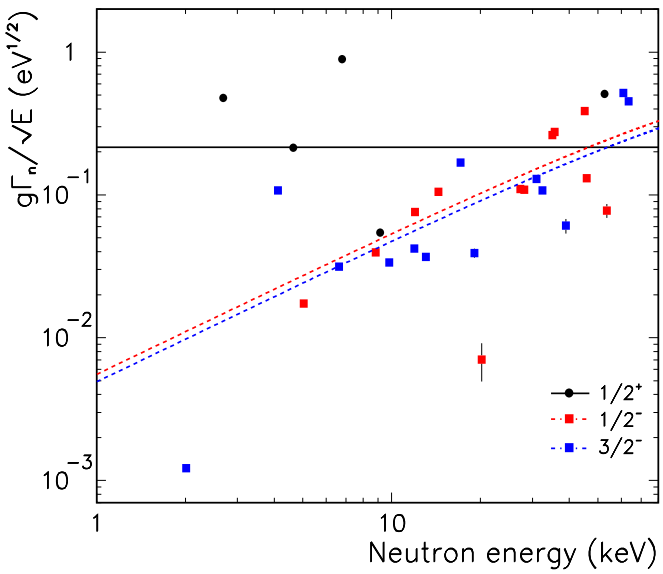

FIG. 8. Neutron widths divided by the square root of the resonance energy as a function of the energy. The expectation values for s- and p-wave resonances are given by full and dashed lines, respectively. Only resonances with Γ_n and J^π listed in Table III are plotted.

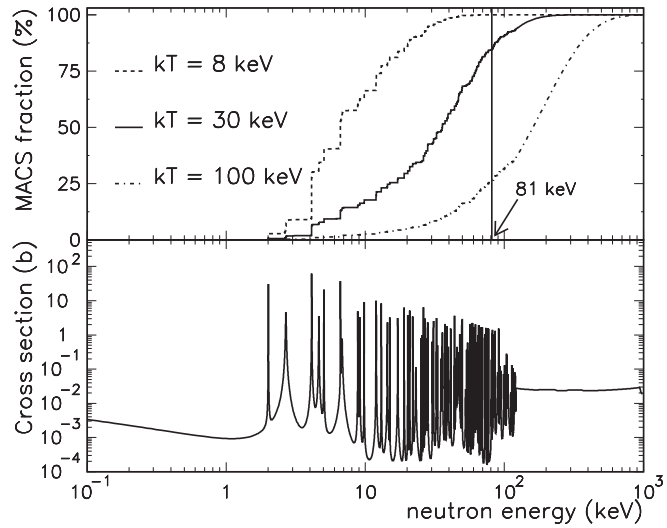

FIG. 9. Upper panel: cumulative contribution to the MACS as a function of incident neutron energy. Lower panel: ^{92}Zr(n, γ) cross section as a function of neutron energy. The cross section was taken from JENDL-4.0 [42].

expected level spacing, neutron strength functions, and channel radius as input parameters. In Fig. 8 the neutron width divided by the square root of the energy is plotted as a function of the resonance energy. The figure indicates that, with the exception of a few strong low energy s-wave resonances, an unambiguous ℓ assignment based on the neutron widths is not possible.

B. Maxwellian averaged cross sections

The s-process production of Zr occurs predominantly in thermally pulsing low mass AGB stars, where neutrons are released by (α, n) reactions with ^{13}C and ^{22}Ne at average energies corresponding to $kT = 8$ keV and $kT = 23$ keV, respectively. In the mass region $56 \leqslant A \lesssim 90$ extreme temperatures near 1 GK also have to be considered. These temperatures are reached during carbon shell burning in massive stars. To calculate the corresponding MACSs in such a wide temperature range, energy dependent capture cross sections for incident neutron energies from 100 eV to at least 500 keV are required. The expected contribution of the ^{92}Zr(n, γ) cross section to the MACSs for $kT = 8$, 30, and 100 keV is shown in Fig. 9. This figure plots the cumulative contributions of the ^{92}Zr(n, γ) cross section to the MACSs as a function of incident neutron energy. The contribution from resonances with an energy below 81 keV to the MACSs with $kT = 8$ and 30 keV is expected to be very close to 100% and higher than 80%, respectively.

The contribution to the MACSs derived from the observed resonances listed in Table III is given in the second column of Table III. Since for some resonances not all resonance parameters can be determined from the measured transmissions and capture yields, we calculated the contribution of each resonance to the MACS from its capture kernel and corresponding low-energy $1/v$ cross section, effectively replacing the numerical integration [55,56]. This $1/v$ contribution is normalized to a thermal cross section of 37 mb as determined in Sec. IV. The contribution of negative resonance is at most 0.04 mb (for $kT = 5$ keV) and is included in the second column of Table III.

In Table III we also list separately the contribution of the DRC due to p waves. An s-wave DRC contribution is unlikely to take place as there are very few negative-parity states in ^{93}Zr. For the keV neutron energy region, the p-wave component of the DRC can be calculated considering a Woods-Saxon shape for the $n + {}^{92}$Zr interaction [43]. It has been estimated that the DRC contribution to the MACS is negligible for low energies, while becoming significant (up to 20%) for temperatures higher than 100 keV.

To estimate the total MACS the contribution for incident neutron energies higher than 81 keV has to be accounted for. This missing contribution was estimated using the ^{92}Zr(n, γ) cross section recommended in ENDF/B-VIII.0 [57], JEFF-3.3 [58], and JENDL-4.0 [42]. The results of these calculations are reported in Table III. The MACS derived from data in evaluated data libraries were obtained by processing data with the NJOY tool [59].

In the last column of Table III a calculation of the total MACS is given. The contribution obtained from the kernels, $1/v$ component, and negative resonance is complemented with the result of the DRC calculation and the capture cross section in ENDF/B-VIII.0 for energies above 81 keV. The table provides MACS from $kT = 5$ to 100 keV and includes MACSs for typical s-process conditions, i.e., $kT = 8$ and 23 keV for the main component and $kT = 90$ keV for the weak component. The uncertainty is the combined uncertainty due to aforementioned components. A 15% of uncertainty was

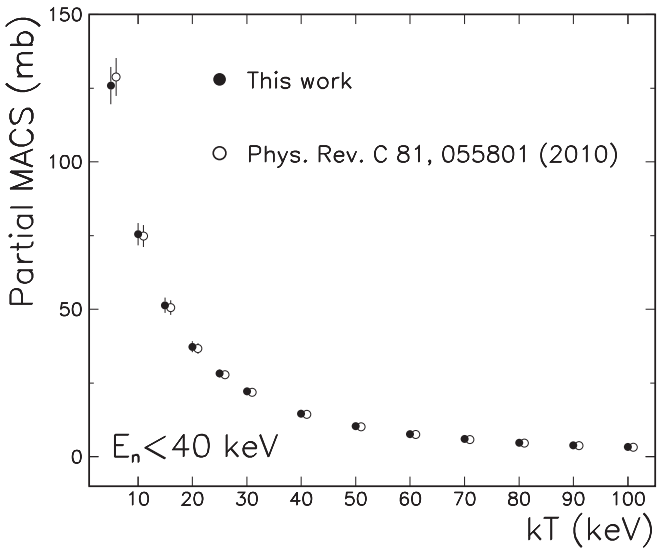

FIG. 10. Contribution to the MACS due to resonances with energy lower than 40 keV. The contributions derived from parameters obtained in this work (full circles) are compared with those derived from parameters in Ref. [15] (open circles). To avoid an overlap of points the values corresponding to the data of Ref. [15] were displaced along the x axis by 1 keV.

assumed for both the DRC component and the cross section recommended in ENDF/B-VIII.0.

The MACS with $kT = 30$ keV is often used to compare results of different MACS estimations; the corresponding values are 36.7(17), 38.9(18), and 39.5(18) mb when using JENDL-4.0, ENDF/B-VIII.0, and JEFF-3.3 cross sections for $E_n >$ 81 keV, respectively. These values are in agreement with the MACS of 34(6) mb measured by Macklin and Gibbons [11] and 33(4) mb derived from the resonance parameters of Boldeman *et al.* [9], after applying the correction factor reported in Ref. [18]. The good agreement with the data obtained from previous measurements at n_TOF is illustrated in Fig. 10. This figure shows the contribution to the MACSs only due to the experimentally observed resonances with energy below 40 keV.

Figure 11 shows the energy dependence of the total MACS from Table III. This energy dependence is compared with the MACSs calculated from the ^{92}Zr(n,γ) cross section recommended in ENDF/B-VIII.0, JEFF-3.3, and JENDL-4.0, and the MACSs taken from the KADoNiS database [60]. Up to $kT \approx 15$ keV, the results obtained in this work are in very good agreement with those of ENDF/B-VIII.0 and KADoNiS [60]. The difference with JENDL-4.0 and JEFF-3.3 is primarily due to the difference in parameters for the resonances at 2685, 4116, 6632, and 6795 eV. The results in Fig. 12 and Table III reveal that the contribution of the evaluations for incident neutron energies above 81 keV produces significantly different MACS for high kT values.

Abundance ratios of Zr isotopes in presolar SiC grains from ancient AGB stars can be experimentally determined with an uncertainty of less than 0.2%. In the theoretical calculations based on a low mass AGB stellar model proposed by Lugaro *et al.* [7], the ^{92}Zr(n,γ) cross section data of

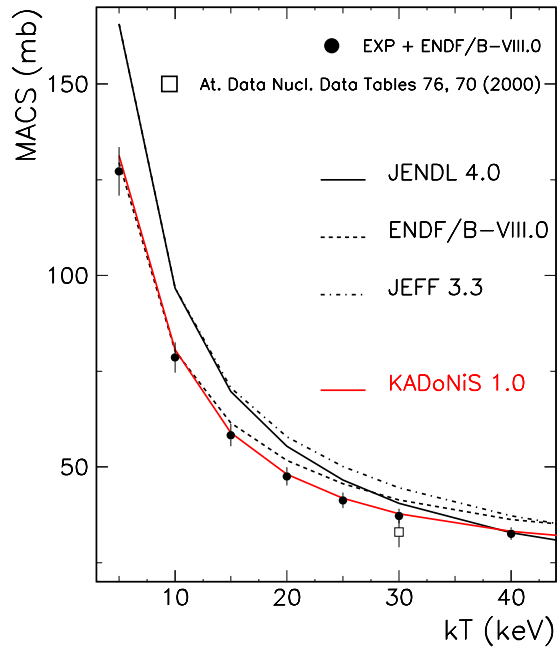

FIG. 11. The total MACSs as a function of kT as given in Table III (full circles) are compared with the compilation from Bao *et al.* [61], the data in KADoNiS [60], and MACSs calculated using the ENDF/B-VIII.0, JEFF-3.3, and JENDL-4.0 libraries.

Ref. [15] had to be reduced by 20% to arrive at a good agreement between the calculated and experimentally determined ^{92}Zr / ^{94}Zr abundance ratio. As we confirm the ^{92}Zr(n,γ)

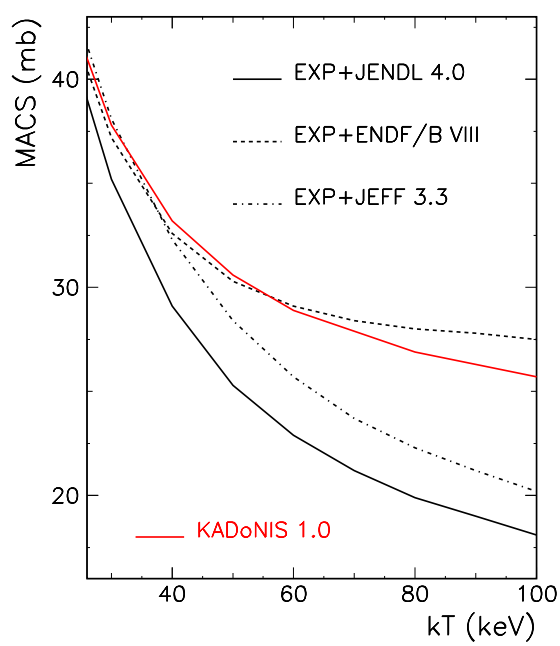

FIG. 12. The MACSs for $kT > 30$ keV obtained by complementing the experimental data from this work with contributions for $E_n > 81$ keV using the ENDF/B-VIII.0, JEFF-3.3, and JENDL-4.0 libraries. These MACSs are compared with the one in the KADoNiS database [60] (red).

MACS of Ref. [15], see Fig. 10, the difference could be due to a problem with the ^{94}Zr(n, γ) cross section. However, since the estimated abundance ratio of the other Zr isotopes and ^{94}Zr are in agreement with the experimental data, this would imply that the capture cross sections for the other isotopes suffer from a similar bias effect. Hence, the problem seems not to be due to these cross sections. Unexpected r-process contributions or shortcomings in the stellar model such as the influence of magnetic fields can also explain the difference between calculated and experimentally determined ^{92}Zr / ^{94}Zr abundance ratio, as discussed in Refs. [62,63].

VII. CONCLUSIONS

High resolution cross section measurements were carried out at the time-of-flight facilities GELINA and n_TOF using metallic samples of enriched ^{92}Zr. The transmission data and capture yields obtained at the GELINA facility were complemented in a resonance shape analysis with the capture yield obtained at n_TOF. The REFIT code was used to derive resonance parameters of ^{92}Zr for neutron energies up to 81 keV by a fit to the transmissions and capture yields obtained at GELINA. The resulting parameters are fully consistent with the capture yield derived from the experiments at n_TOF, which were analyzed with SAMMY. Thanks to the combination of experimental data obtained in different experimental conditions at two TOF-facilities, the bias effects due to the TOF response function, the normalization of capture data, and the background contributions are largely reduced. The obtained resonance strengths and capture kernels are on average in good agreement with those reported in previous works. The resonance parameters were used to derive neutron strength functions, average radiative widths, and average resonance spacings.

The MACSs at $kT = 30$ keV derived from the parameters obtained in this work are fully consistent with experimental data reported in the literature [9,15]. For MACSs with higher kT, the present data have to be complemented with capture cross sections for neutron energies above 81 keV. Unfortunately, recommended cross sections for these energies are very different. Results obtained in this work were used in AGB stellar model calculations to study experimentally observed abundance ratios for Zr isotopes. The previously reported discrepancy between experimental and calculated ^{92}Zr / ^{94}Zr abundance ratio remains.

The results obtained in this work call for a new evaluation based on a resonance shape analysis combining the transmission data and capture yields obtained in this work with the transmission data and capture yield previously obtained by Boldeman *et al.* at the ORELA facility. In addition, improved capture cross section data are required for a new evaluation of the ^{92}Zr(n, γ) cross section in the energy region above 80 keV.

ACKNOWLEDGMENTS

We are indebted to the anonymous referees for a careful reading of the manuscript and constructive remarks. This research was funded by the European Community Seventh Framework Programme FP7/2007-2011 under the Project CHANDA (Grant No. 605203), by the European Commission within HORIZON2020 via the EURATOM project EUFRAT for transnational access and by the funding agencies of the participating institutes.

[1] G. Wallerstein, I. Iben, P. Parker, A. M. Boesgaard, G. M. Hale, A. E. Champagne, C. A. Barnes, F. Käppeler, V. V. Smith, R. D. Hoffman, F. X. Timmes, C. Sneden, R. N. Boyd, B. S. Meyer, and D. L. Lambert, Rev. Mod. Phys. **69**, 995 (1997).
[2] E. M. Burbidge, G. R. Burbidge, W. A. Fowler, and F. Hoyle, Rev. Mod. Phys. **29**, 547 (1957).
[3] P. A. Seeger, W. A. Fowler, and D. D. Clayton, Astrophys. J. Suppl. Ser. **11**, 121 (1965).
[4] E. Zinner, Publ. Astron. Soc. Australia **25**, 7 (2008).
[5] A. M. Davis, Proc. Natl. Acad. Sci. U.S.A. **108**, 48 (2011).
[6] M. Lugaro, *Stardust from Meteorites: An Introduction to Presolar Grains* (World Scientific, Singapore 2005).
[7] M. Lugaro, G. Tagliente, A. I. Karakas, P. M. Milazzo, F. Käppeler, A. M. Davis, and M. R. Savina, Astrophys. J. **780**, 95 (2014).
[8] S. Leray, Nucl. Instrum. Methods B **113**, 495 (1996).
[9] J. W. Boldeman, A. R. de L. Musgrove, B. J. Allen, J. A. Harvey, and R. L. Macklin, Nucl. Phys. A **269**, 31 (1976).
[10] S. S. Moskalev, H. V. Muradian, and Y. V. Adamchuk, Nucl. Phys. **53**, 667 (1964).
[11] R. L. Macklin and J. H. Gibbons, Astrophys. J. **149**, 577 (1967).
[12] W. M. Good and H. Kim, Phys. Rev. **165**, 1329 (1968).
[13] Z. M. Bartolome, R. W. Hockenbury, W. R. Moyer, J. R. Tatarczuk, and R. C. Block, Nucl. Sci. Eng. **37**, 137 (1969).
[14] K. Ohgama, M. Igashira, and T. Ohsaki, J. Nucl. Sci. Technol. **42**, 333 (2005).
[15] G. Tagliente *et al.* (n_TOF Collaboration), Phys. Rev. C **81**, 055801 (2010).
[16] S. F. Mughabghab, *Atlas of Neutron Resonances, Volume 1: Resonance Properties and Thermal Cross Sections Z= 1–60* (Elsevier, Amsterdam, 2018).
[17] S. Sukhoruchkin, Z. Soroko, P. Schillebeeckx, B. Becker, H. Harada, and S. Kopecky, *Neutron Resonance Parameters* (Springer, Berlin, 2015).
[18] B. J. Allen, J. W. Boldeman, and R. L. Macklin, Nucl. Sci. Eng. **82**, 230 (1982).
[19] P. Schillebeeckx, B. Becker, Y. Danon, K. Guber, H. Harada, J. Heyse, A. R. Junghans, S. Kopecky, C. Massimi, M. C. Moxon, N. Otuka, I. Sirakov, and K. Volev, Nucl. Data Sheets **113**, 3054 (2012).
[20] C. Guerrero *et al.* (n_TOF Collaboration), Eur. Phys. J. A **49**, 27 (2013).
[21] U. Abbondanno *et al.*, CERN n_TOF facility: Performance report, CERN Technical Report No, CERN-SL-2002-053 ECT, 2003 (unpublished).
[22] C. Borcea *et al.*, Nucl. Instrum. Methods Phys. Res., Sect. A **513**, 524 (2003).
[23] S. Marrone *et al.*, Nucl. Instrum. Methods Phys. Res., Sect. A **517**, 389 (2004).

[24] W. Mondelaers and P. Schillebeeckx, Notizario Neutroni e Luce di Sincrotrone **11**, 19 (2006).

[25] D. Tronc, J. M. Salomé, and K. H. Böckhoff, Nucl. Instrum. Methods Phys. Res., Sect. A **228**, 217 (1985).

[26] J. M. Salome and R. Cools, Nucl. Instrum. Methods **179**, 13 (1981).

[27] R. L. Macklin and J. H. Gibbons, Phys. Rev. **159**, 1007 (1967).

[28] A. Borella, G. Aerts, F. Gunsing, M. Moxon, P. Schillebeeckx, and R. Wynants, Nucl. Instrum. Methods Phys. Res., Sect. A **577**, 626 (2007).

[29] C. Lampoudis, S. Kopecky, O. Bouland, F. Gunsing, G. Noguere, A. J. M. Plompen, C. Sage, P. Schillebeeckx, and R. Wynants, Eur. Phys. J. Plus **128**, 86 (2013).

[30] H. Tsuchiya, H. Harada, M. Koizumi, F. Kitatani, J. Takamine, M. Kureta, H. Iimura, A. Kimura, B. Becker, S. Kopecky, K. Kauwenberghs, W. Mondelaers, and P. Schillebeeckx, Nucl. Instrum. Methods Phys. Res., Sect. A **767**, 364 (2014).

[31] B. Becker, S. Kopecky, H. Harada, and P. Schillebeeckx, Eur. Phys. J. Plus **129**, 58 (2014).

[32] M. C. Moxon and J. B. Brisland, GEEL REFIT, A least squares fitting program for resonance analysis of neutron transmission and capture data computer code, AEA Technical Report No. AEA-InTec-0630, 2008 (unpublished).

[33] R. L. Macklin, J. Halperin, and R. R. Winters, Phys. Rev. C **11**, 1270 (1975).

[34] N. Yamamuro, T. Hayase, T. Doi, Y. Fujita, K. Kobayashi, and R. C. Block, Nucl. Instrum. Methods **133**, 531 (1976).

[35] C. Massimi, A. Borella, S. Kopecky, C. Lampoudis, P. Schillebeeckx, M. C. Moxon, and G. Vannini, J. Kor. Phys. Soc. **59**, 1689 (2011).

[36] F. G. Perey, in *Proceedings of the International Conference on Nuclear Data for Basic and Applied Science* (Santa Fe, New Mexico, 1985), pp. 1523–1528.

[37] C. Lampoudis, S. Kopecky, P. Schillebeeckx, P. Siegler, and K. Guber, J. Korean Phys. Soc. **59**, 1860 (2011).

[38] C. W. Reich and M. S. Moore, Phys. Rev. **111**, 929 (1958).

[39] E. P. Wigner and L. Eisenbud, Phys. Rev. **72**, 29 (1947).

[40] N. M. Larson, Updated users' guide for SAMMY: Multilevel R-matrix fits to neutron data using Bayes' equations, Oak Ridge National Laboratory Technical Report No. ORNL/TM-9179/R8, 2008 (unpublished).

[41] M. Flaska, A. Borella, D. Lathouwers, L. C. Mihailescu, W. Mondelaers, A. J. M. Plompen, H. van Dam, and T. H. J. J. van der Hagen, Nucl. Instrum. Methods Phys. Res., Sect. A **531**, 394 (2004).

[42] K. Shibata, O. Iwamoto, T. Nakagawa, N. Iwamoto, A. Ichihara, S. Kuneida, S. Chiba, K. Furutaka, N. Otuka, T. Ohsawa, T. Murata, H. Matsunobu, A. Zukeran, S. Kamada, and J.-I. Katakura, J. Nucl. Sci. Technol. **48**, 1 (2011).

[43] A. Mengoni, T. Otsuka, and M. Ishihara, Phys. Rev. C **52**, R2334 (1995).

[44] H. Derrien, L. C. Leal, N. M. Larson, and A. Courcelle, Neutron Resonance Parameters of ^{238}U and the Calculated Cross Sections from the Reich-Moore Analysis of Experimental Data in the Neutron Energy Range from 0 keV to 20 keV, Oak Ridge National Laboratory Technical Report No. ORNL/TM-2005/241, 2005 (unpublished).

[45] C. Massimi *et al.* (n_TOF Collaboration), Phys. Rev. C **81**, 044616 (2010).

[46] H. Pomerance, Phys. Rev. **88**, 412 (1952).

[47] L. Koester, K. Knopf, and W. Waschkowski, Z. Phys. A **301**, 215 (1981).

[48] R. L. Macklin and B. J. Allen, Nucl. Instrum. Methods **91**, 565 (1971).

[49] M. J. Kenny, M. L. Stelts, and R. E. Chrien, in *Proceedings, Neutron Gamma Ray Spectroscopy and Related Topics* (Brookhaven National Laboratory, Upton, New York, 1978), pp. 646–648.

[50] M. Mastromarco *et al.* (n_TOF Collaboration), Eur. Phys. J. A **55**, 9 (2019).

[51] L. M. Bollinger and G. E. Thomas, Phys. Rev. **171**, 1293 (1968).

[52] L. Zanini, F. Corvi, H. Postma, and F. Bečvář, Phys. Rev. C **61**, 054616 (2000).

[53] F. Gunsing, A. Leprêtre, C. Mounier, C. Raepsaet, A. Brusegan, and E. Macavero, Phys. Rev. C **61**, 054608 (2000).

[54] C. E. Porter and R. G. Thomas, Phys. Rev. **104**, 483 (1956).

[55] R. L. Macklin and J. H. Gibbons, Rev. Mod. Phys. **37**, 166 (1965).

[56] H. Beer, F. Voss, and R. R. Winters, Astrophys. J. Suppl. Ser. **80**, 403 (1992).

[57] D. Brown *et al.*, Nucl. Data Sheets **148**, 1 (2018), Special Issue on Nuclear Reaction Data.

[58] A. J. M. Plompen *et al.*, Eur. Phys. J. A **56**, 181 (2020).

[59] R. E. MacFarlane and A. C. Kahler, Nucl. Data Sheets **111**, 2739 (2010).

[60] I. Dillmann, M. Heil, F. Käppeler, R. Plag, T. Rauscher, and F.-K. Thielemann, in *Capture Gamma-Ray Spectroscopy and Related Topics*, edited by A. Woehr and A. Aprahamian (AIP, New York, 2005), p. 123.

[61] Z. Y. Bao, H. Beer, F. Käppeler, F. Voss, K. Wisshak, and T. Rauscher, Atomic Data Nucl. Data Tables **76**, 70 (2000).

[62] D. Vescovi, S. Cristallo, M. Busso, and N. Liu, Astrophys. J. Lett. **897**, L25 (2020).

[63] M. Busso, D. Vescovi, S. Palmerini, S. Cristallo, and V. Antonuccio-Delogu, Astrophys. J. **908**, 55 (2021).